

# Octupolar edge state in an $e_g$ orbital system on a square lattice

Katsunori Kubo

Advanced Science Research Center, Japan Atomic Energy Agency, Tokai, Ibaraki 319-1195, Japan

(Dated: August 14, 2024)

A tight-binding model for  $e_g$  orbitals on a square lattice is investigated. We consider only the nearest-neighbor hopping and the model is characterized by two hopping parameters,  $t_1$  and  $t_2$ . There are Dirac points in the electronic band structure and the type of the Dirac points (type-I or type-II) depends on the ratio  $t_2/t_1$ . For the case of the type-I Dirac points, edge states appear for a lattice with edges perpendicular to the [11] direction. The edge states at a certain momentum along the edges have octupole moments with opposite signs between the right and left edges. Thus, these edge states can be called helical octupolar edge states. This study bridges the research fields of topological phenomena and multipole physics.

## I. INTRODUCTION

Topological semimetals, characterized by the presence of Dirac or Weyl points (topological nodal points) in their electronic band structures, have garnered significant attention due to their intriguing physical properties [1–4]. A topological nodal point is defined as a point where the upper and lower bands touch each other, possessing topological protection. A Dirac point exhibits spin degeneracy, while a Weyl point does not. Realizing such topological nodal points necessitates at least two bands. In systems with two sites in a unit cell, two bands are present. Graphene is a prime example of such a system, exhibiting Dirac points [1, 2]. Alternatively, the spin degrees of freedom can be used to achieve two bands. For instance, the Rashba spin-orbit coupling [5] lifts the spin degeneracy of a band, except at certain  $\mathbf{k}$  points where the degeneracy is preserved by time-reversal symmetry, resulting in Weyl points [6].

In this study, we explore an alternative approach to achieve two bands and Dirac points by exploiting the orbital degrees of freedom. As a representative two-orbital system, we investigate a model for the  $e_g$  orbitals of  $d$  electrons. Notably, type-II Dirac points have been observed in  $e_g$  orbital systems, including an  $e_g$  orbital model [7], a cuprate superconductor [8], and a LaAlO<sub>2</sub>/LaNiO<sub>3</sub>/LaAlO<sub>3</sub> quantum well [9]. A type-II Dirac point is characterized by the touching of upper and lower bands, with electron and hole pockets extending from it even when the Fermi level is situated at this point [10] [see, Fig.1(f)]. A type-I Dirac point also involves the touching of upper and lower bands, but in this case, the Fermi surface vanishes around it when the Fermi level is located at this point [see, Fig.1(h)]. Traditionally, only type-I Dirac points were referred to as Dirac points until the term “type-II Dirac point” was introduced [10]. Despite the anticipation of several intriguing features, phenomena arising from topological signatures might be obscured by the presence of finite density states at the Fermi level in type-II Dirac point cases.

Here, we consider a tight-binding model for the  $e_g$  orbitals on a square lattice with nearest-neighbor hopping in a general form. This model contains two hop-

ping parameters. Such a simple tight-binding model, like the Kane-Mele model for topological insulators [11], the tight-binding model for graphene possessing Dirac points [12], and the Rashba-Hubbard model for a Weyl semimetal [6], is invaluable for exploring and demonstrating topological phenomena. By tuning the ratio of the two parameters, we demonstrate the emergence of type-I Dirac points in the  $e_g$  orbital system. Furthermore, we explore the emergence of edge states unique to the type-I Dirac point cases. Specifically, we observe that these edge states have octupolar moments, with opposite signs between the left and right edges, at a certain momentum along the edges.

## II. MODEL

In this study, we do not consider a magnetic field or magnetic order. Hence, we can disregard the spin degrees of freedom and simplify the model to a spinless one for the  $e_g$  orbitals. The model Hamiltonian on a square lattice with nearest-neighbor hopping is represented as follows:

$$H = \sum_{\tau\tau'} c_{\mathbf{k}\tau}^\dagger \epsilon_{\tau\tau'}(\mathbf{k}) c_{\mathbf{k}\tau'}, \quad (1)$$

where  $c_{\mathbf{k}\tau}$  is the annihilation operator for an electron with momentum  $\mathbf{k}$  and orbital  $\tau$ . Here,  $\tau = 1$  denotes the  $x^2 - y^2$  orbital, and  $\tau = 2$  denotes the  $3z^2 - r^2$  orbital. The matrix elements of the Hamiltonian are given by [13, 14]

$$\epsilon_{11}(\mathbf{k}) = \frac{1}{2}[3(dd\sigma) + (dd\delta)](c_x + c_y) + \frac{\Delta}{2}, \quad (2)$$

$$\epsilon_{22}(\mathbf{k}) = \frac{1}{2}[(dd\sigma) + 3(dd\delta)](c_x + c_y) - \frac{\Delta}{2}, \quad (3)$$

$$\epsilon_{12}(\mathbf{k}) = \epsilon_{21}(\mathbf{k}) = -\frac{\sqrt{3}}{2}[(dd\sigma) - (dd\delta)](c_x - c_y), \quad (4)$$

where  $c_\mu = \cos k_\mu$  with  $\mu = x$  or  $y$ , and  $\Delta$  represents the difference in the onsite energy level between the two orbitals. The lattice constant is set as unity here. The quantities  $(dd\sigma)$  and  $(dd\delta)$  denote the two-center integrals [15]. This model can be regarded as a model for  $\Gamma_8$

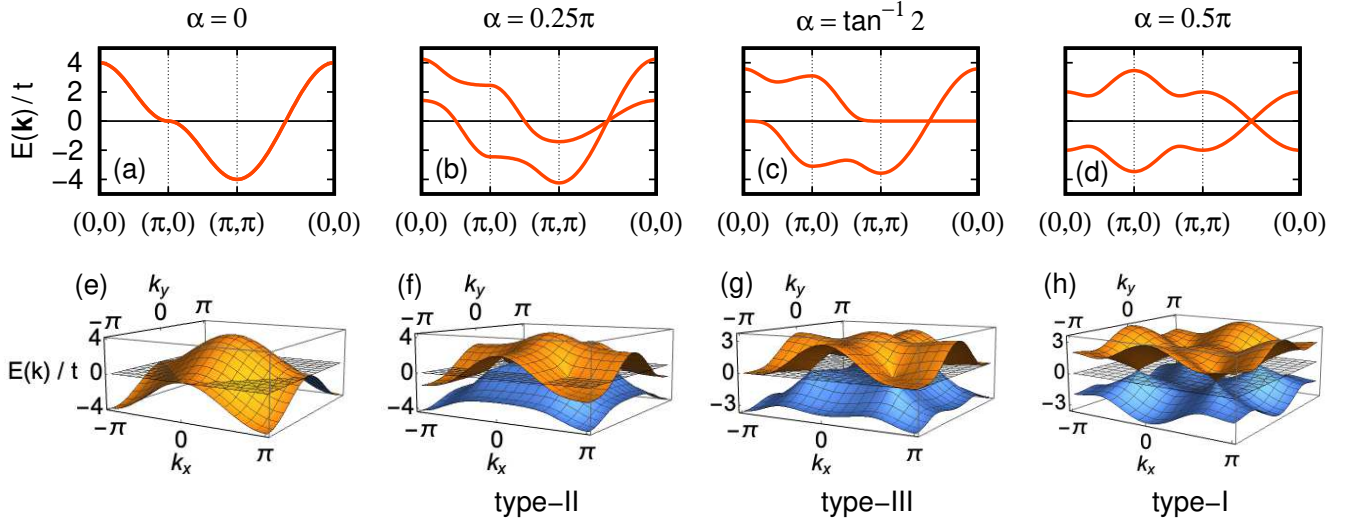


FIG. 1. Energy dispersion for  $\Delta = 0$ . Energy dispersion along symmetric directions: (a) for  $\alpha = 0$  ( $t_2 = 0$ ), (b) for  $\alpha = 0.25\pi$  ( $t_2 = t_1$ ), (c) for  $\alpha = \tan^{-1} 2$  ( $= 0.3524\pi$ ,  $t_2 = 2t_1$ ), and (d) for  $\alpha = 0.5\pi$  ( $t_1 = 0$ ). Lower panels show energy dispersion in the entire Brillouin zone: (e) for  $\alpha = 0$ , (f) for  $\alpha = 0.25\pi$ , (g) for  $\alpha = \tan^{-1} 2$ , and (h) for  $\alpha = 0.5\pi$ . The zero-energy plane is drawn in these figures to distinguish the types of Dirac points clearly.

orbitals of  $f$  electrons by replacing  $(dd\sigma)$  with  $[3(ff\sigma) + 4(ff\pi)]/7$  and  $(dd\delta)$  with  $[(ff\pi) + 5(ff\delta) + 15(ff\phi)]/21$ . Since it is a two-orbital model, the matrix  $\epsilon(\mathbf{k})$  can be expressed using the Pauli matrices as

$$\begin{aligned} \epsilon(\mathbf{k}) &= \frac{1}{2}[\epsilon_{11}(\mathbf{k}) + \epsilon_{22}(\mathbf{k})]\sigma^0 \\ &+ \frac{1}{2}[\epsilon_{11}(\mathbf{k}) - \epsilon_{22}(\mathbf{k})]\sigma^z + \epsilon_{12}(\mathbf{k})\sigma^x \quad (5) \\ &= h_0(\mathbf{k})\sigma^0 + h_x(\mathbf{k})\sigma^x + h_z(\mathbf{k})\sigma^z, \end{aligned}$$

where  $\sigma^\mu$  represents the  $\mu$  component of the Pauli matrix, and  $\sigma^0$  is defined as the unit matrix. The coefficients are given by

$$\begin{aligned} h_0(\mathbf{k}) &= [\epsilon_{11}(\mathbf{k}) + \epsilon_{22}(\mathbf{k})]/2 \\ &= [(dd\sigma) + (dd\delta)](c_x + c_y) \quad (6) \\ &= 2t_1(c_x + c_y), \end{aligned}$$

$$\begin{aligned} h_x(\mathbf{k}) &= \epsilon_{12}(\mathbf{k}) = \epsilon_{21}(\mathbf{k}) \\ &= -\frac{\sqrt{3}}{2}[(dd\sigma) - (dd\delta)](c_x - c_y) \quad (7) \\ &= -\sqrt{3}t_2(c_x - c_y), \end{aligned}$$

$$\begin{aligned} h_z(\mathbf{k}) &= [\epsilon_{11}(\mathbf{k}) - \epsilon_{22}(\mathbf{k})]/2 \\ &= \frac{1}{2}[(dd\sigma) - (dd\delta)](c_x + c_y) + \frac{\Delta}{2} \quad (8) \\ &= t_2(c_x + c_y) + \Delta/2, \end{aligned}$$

where we have defined

$$t_1 = [(dd\sigma) + (dd\delta)]/2, \quad (9)$$

$$t_2 = [(dd\sigma) - (dd\delta)]/2. \quad (10)$$

We can assume  $t_1 \geq 0$  and  $t_2 \geq 0$  without loss of generality. Then, we parameterize them as

$$t_1 = t \cos \alpha, \quad (11)$$

$$t_2 = t \sin \alpha, \quad (12)$$

with  $t > 0$  and  $0 \leq \alpha \leq \pi/2$ .

This model has been investigated in various contexts with different values of  $\alpha$ . The model at  $\alpha = \pi/4$  [ $t_1 = t_2$ ,  $(dd\delta) = 0$ , see Fig. 1(b)] has been used as a model for perovskite manganites [16] and as a model for  $\Gamma_8$  orbitals of  $f$  electrons, considering only  $(ff\sigma)$  [17–28]. From this model, an effective Hamiltonian in the strong coupling limit is derived, and frustration arising from the orbital anisotropy is discussed [29–33]. A similar frustrated model is known as the Kitaev model and has been intensively studied [34, 35]. By using the model at  $\alpha = 0$  [ $t_2 = 0$ ,  $(dd\delta) = (dd\sigma)$ , see Fig. 1(a)], the possible anisotropic superconducting pairing originating from the orbital anisotropy of  $e_g$  orbitals was discussed [36]. Such anisotropic superconductivity has been discussed for the  $f$ -electron system  $\text{PrT}_2\text{X}_{20}$  (where T denotes a transition metal element and X denotes Zn or Al) [25–28]. The model at  $\alpha = \pi/2$  [ $t_1 = 0$ ,  $(dd\delta) = -(dd\sigma)$ , see Fig. 1(d)] near half-filling exhibits pocket Fermi surfaces around  $(\pm\pi/2, \pm\pi/2)$ . Suppose a superconducting pair is composed of electrons on the same Fermi pocket. In that case, the superconducting pair has a finite total momentum, resembling the Fulde-Ferrell-Larkin-Ovchinnikov state [37, 38], even without a magnetic field similar to the  $\eta$ -pairing state [39]. This possibility has been investigated in Refs. [13, 14].

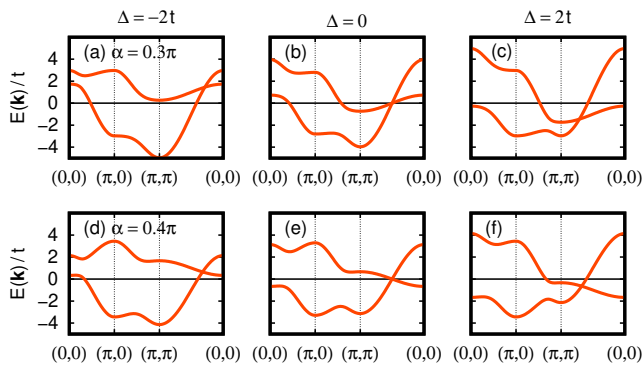


FIG. 2. Energy dispersion for  $\Delta = -2t, 0,$  and  $2t$  along symmetric directions. Upper panels show energy dispersion for  $\alpha = 0.3\pi$  (a) for  $\Delta = -2t$ , (b) for  $\Delta = 0$ , and (c) for  $\Delta = 2t$ . Lower panels show energy dispersion for  $\alpha = 0.4\pi$  (d) for  $\Delta = -2t$ , (e) for  $\Delta = 0$ , and (f) for  $\Delta = 2t$ .

### III. ENERGY BANDS

The energy dispersion of the model is given by

$$E(\mathbf{k}) = h_0(\mathbf{k}) \pm \sqrt{h_x^2(\mathbf{k}) + h_z^2(\mathbf{k})} \quad (13)$$

$$= h_0(\mathbf{k}) \pm h(\mathbf{k}).$$

The two bands touch each other at the Dirac points, where  $h(\mathbf{k}) = 0$ .

In Fig. 1, we show the energy dispersion for  $\Delta = 0$  for some values of  $\alpha$ . The bandwidth  $W$  varies non-monotonically with  $\alpha$ :  $W = 8t$  at  $\alpha = 0$  [Fig. 1(a)],  $W$  exceeds  $8t$ , for example, at  $\alpha = 0.25\pi$  [Fig. 1(b)], and  $W = 4\sqrt{3}t$  at  $\alpha = 0.5\pi$  [Fig. 1(d)]. Note that hybridization between the  $x^2 - y^2$  and  $3z^2 - r^2$  orbitals is forbidden along the  $k_x = k_y$  line due to mirror symmetry [7, 8]. For the half-filled case with  $\Delta = 0$ , the Fermi level is zero due to electron-hole symmetry and the Dirac points are always located at the Fermi level.

The two bands are degenerate for  $\alpha = 0$  [ $t_2 = 0$ , Figs. 1(a) and 1(e)]. For  $\alpha \neq 0$ , Dirac points emerge at  $(\pm\pi/2, \pm\pi/2)$ , and the type of the Dirac points depends on  $\alpha$ . For  $\alpha < \tan^{-1} 2$  [Figs. 1(b) and 1(f)], they are of type-II, where the two Fermi surfaces touch each other at the Dirac points for half-filling. For  $\alpha > \tan^{-1} 2$  [Figs. 1(d) and 1(h)], they are of type-I, and the Fermi surface disappears for half-filling. The disappearance of the Fermi surface at  $\alpha = 0.5\pi$  was already pointed out in Refs. [13, 14]. At the border  $\alpha = \tan^{-1} 2$  ( $= 0.3524\pi$ ,  $t_2 = 2t_1$ ), a flat dispersion is observed along the  $(0,0)$ - $(\pi, \pi)$  direction [Figs. 1(c) and 1(g)], and the Dirac points are called type-III [40, 41]. For the half-filled case, the change in the type of Dirac points is a Lifshitz transition [42].

The energy dispersions for finite  $\Delta$  are depicted in Fig. 2 for  $\alpha = 0.3\pi$  (type-II Dirac point) and for  $\alpha = 0.4\pi$  (type-I Dirac point). The Dirac point is given by  $k_x = k_y = \cos^{-1}[-\Delta/(4t_2)]$ . Although the position of the

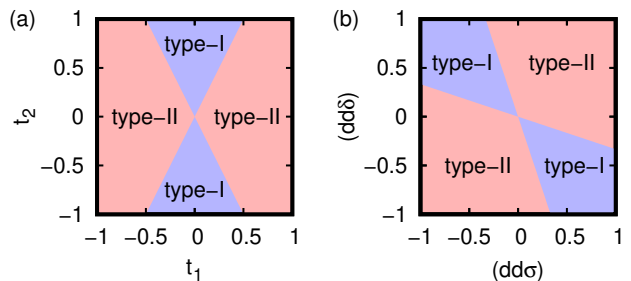


FIG. 3. Regions of the type-I and type-II Dirac semimetals: (a) on the  $t_1$ - $t_2$  plane and (b) on the  $(dd\delta)$ - $(dd\sigma)$  plane. The type of the Dirac points is independent of  $\Delta$ . The energy unit in these figures is arbitrary.

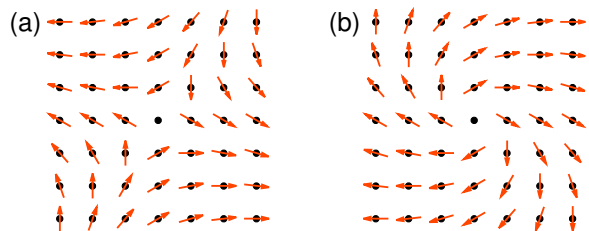


FIG. 4.  $\hat{h}(\mathbf{k})$  (a) around  $\mathbf{k} = (\pi/2, \pi/2)$  and (b) around  $\mathbf{k} = (\pi/2, -\pi/2)$ .

Dirac point shifts from  $(\pi/2, \pi/2)$  for finite  $\Delta$ , the type of the Dirac point remains unchanged. While the energy at the Dirac point deviates from zero for  $\Delta \neq 0$ , it still resides at the Fermi level  $E = -\Delta/\tan\alpha$  for half-filling in the type-I Dirac point cases, maintaining the system semimetallic. On the other hand, in the case of type-II Dirac points, the Dirac points are not aligned with the Fermi level for half-filling when  $\Delta \neq 0$ . For a large level splitting  $|\Delta| > 4t_2$  (not shown), a gap opens between the two bands, leading to the disappearance of the Dirac points.

Figure 3 shows the parameter regions of the type-I and type-II Dirac semimetals on both the  $t_1$ - $t_2$  plane [Fig. 3(a)] and on the  $(dd\sigma)$ - $(dd\delta)$  plane [Fig. 3(b)]. The type of the Dirac points depends solely on the ratio  $t_2/t_1$  or  $(dd\delta)/(dd\sigma)$ , making it unnecessary to specify the energy unit in these figures. On the  $t_1$ - $t_2$  plane, the boundaries are given by  $t_2 = \pm 2t_1$ . On the  $(dd\sigma)$ - $(dd\delta)$  plane, the boundaries are given by  $(dd\delta) = -(dd\sigma)/3$  and  $(dd\delta) = -3(dd\sigma)$ . For perovskite manganites, models with  $(dd\delta) = 0$  are commonly employed, resulting in type-II Dirac points. However, it is worth noting that the condition  $|(dd\delta)| > |(dd\sigma)|/3$  with opposite signs for  $(dd\delta)$  and  $(dd\sigma)$  is not unrealistic, indicating the possibility of type-I Dirac points emerging in  $e_g$  orbital systems.

Figure 4 shows the normalized vector field  $\hat{h}(\mathbf{k}) = \mathbf{h}(\mathbf{k})/h(\mathbf{k}) = [h_x(\mathbf{k}), h_z(\mathbf{k})]/h(\mathbf{k}) = [\hat{h}_x(\mathbf{k}), \hat{h}_z(\mathbf{k})]$  around the Dirac points  $\mathbf{k} = (\pi/2, \pi/2)$  and  $\mathbf{k} = (\pi/2, -\pi/2)$  for  $\Delta = 0$ . The vector  $\hat{h}(\mathbf{k})$  has vortex struc-

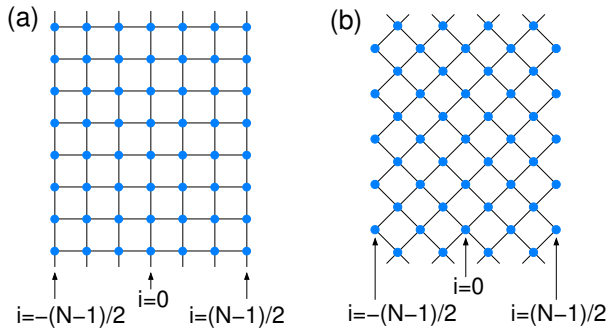


FIG. 5. Lattices with edges. (a) Straight edges. (b) Zigzag edges.  $i$  denotes the label representing positions perpendicular to the edges, and  $N$  is the number of these positions.

tures around the Dirac points. The winding number of a normalized two-component vector field  $\hat{h}(\mathbf{k})$  is [43, 44]

$$w = \oint_C \frac{d\mathbf{k}}{2\pi} \cdot \left[ \hat{h}_x(\mathbf{k}) \nabla \hat{h}_z(\mathbf{k}) - \hat{h}_z(\mathbf{k}) \nabla \hat{h}_x(\mathbf{k}) \right], \quad (14)$$

where  $C$  is a loop enclosing a Dirac point. We obtain  $w = -1$  for  $\mathbf{k} = (\pi/2, \pi/2)$  and  $\mathbf{k} = (-\pi/2, -\pi/2)$  and  $w = 1$  for  $\mathbf{k} = (\pi/2, -\pi/2)$  and  $(-\pi/2, \pi/2)$ .

While the topology of the model is determined solely by  $\mathbf{h}(\mathbf{k})$ ,  $h_0(\mathbf{k})$  affects the existence of the gap of the band projected onto the edge momentum space. Therefore,  $h_0(\mathbf{k})$  is also important for the edge states, as we will see in the next section.

#### IV. EDGE STATES

From the presence of topological defects such as Dirac points, we anticipate the emergence of edge states similar to those observed in a model of graphene [12, 45, 46]. We consider two types of edges: those aligned along the  $y$  direction [straight edges, Fig. 5(a)], and those perpendicular to the [11] direction [zigzag edges, Fig. 5(b)]. We denote the momentum along the edges as  $k$  and the momentum perpendicular to the edges as  $k_\perp$ . To examine the presence of edge states, the winding number  $w(k)$  for a fixed  $k$  is crucial [45, 46]:

$$w(k) = \int_0^{2\pi} \frac{dk_\perp}{2\pi} \left[ \hat{h}_x(\mathbf{k}) \frac{\partial}{\partial k_\perp} \hat{h}_z(\mathbf{k}) - \hat{h}_z(\mathbf{k}) \frac{\partial}{\partial k_\perp} \hat{h}_x(\mathbf{k}) \right]. \quad (15)$$

For the zigzag edges,  $h_x(\mathbf{k}) = -2\sqrt{3}t_2 \sin k \sin k_\perp$  and  $h_z(\mathbf{k}) = 2t_2 \cos k \cos k_\perp + \Delta/2$ , where we have set  $1/\sqrt{2}$  times the bond length as unity here. For simplicity, we evaluate the winding number  $w(k)$  for  $\Delta = 0$ . For the straight edges, we find  $w(k) = 0$  and the edge states will probably be absent. The value of  $w(k)$  can generally change at the Dirac point projected onto the edge momentum space. However, in this case, the Dirac points with opposite winding numbers are projected onto the

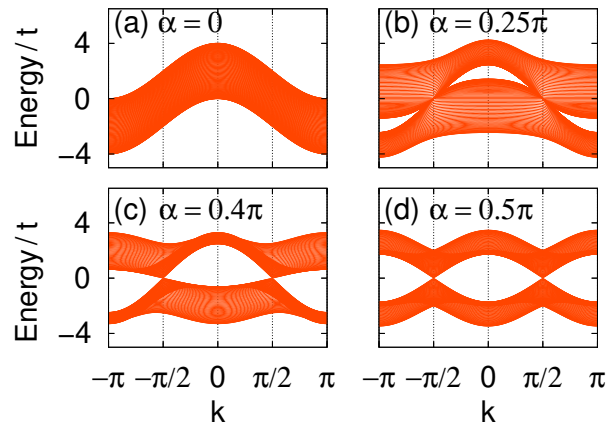


FIG. 6. Energy dispersion at  $\Delta = 0$  for a lattice with straight edges with  $N = 71$ : (a) for  $\alpha = 0$ , (b) for  $\alpha = 0.25\pi$ , (c) for  $\alpha = 0.4\pi$ , and (d) for  $\alpha = 0.5\pi$ .

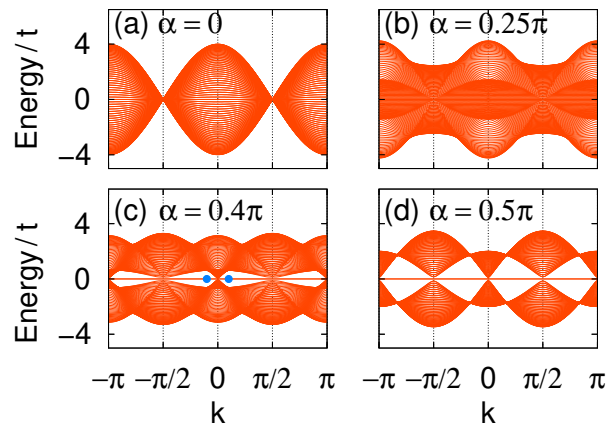


FIG. 7. Energy dispersion at  $\Delta = 0$  for a lattice with zigzag edges with  $N = 71$ : (a) for  $\alpha = 0$ , (b) for  $\alpha = 0.25\pi$ , (c) for  $\alpha = 0.4\pi$ , and (d) for  $\alpha = 0.5\pi$ . The solid circles in (c) indicate edge states in which the multipole density is evaluated in Figs. 9(a) and 9(c).

same momentum  $k = \pm\pi/2$ . Consequently,  $w(k)$  remains zero throughout the edge momentum space. For the zigzag edges, we find  $w(k) = \text{sgn}[\sin(2k)]$  except for  $k = 0, \pm\pi/2$ , and  $\pm\pi$  (projected Dirac points). Hence, edge states should exist, at least without  $t_1$  and  $\Delta$ , except at the projected Dirac points.

To explicitly demonstrate the existence of the edge states, we calculate the energy bands for lattices with finite widths. Figure 6 shows the energy bands for a lattice with straight edges with various values of  $\alpha$  for  $\Delta = 0$ . We notice that all bands are bulk states; that is, no edge state isolated from the bulk states appears. This observation is consistent with  $w(k) = 0$ . We have also calculated the band dispersions for a lattice with straight edges with  $\Delta \neq 0$  (not shown) and found no edge state. In Fig. 7, we show the energy bands for a lattice with zigzag edges with various values of  $\alpha$  for  $\Delta = 0$ . We observe the zero-energy states isolated from the bulk states when the

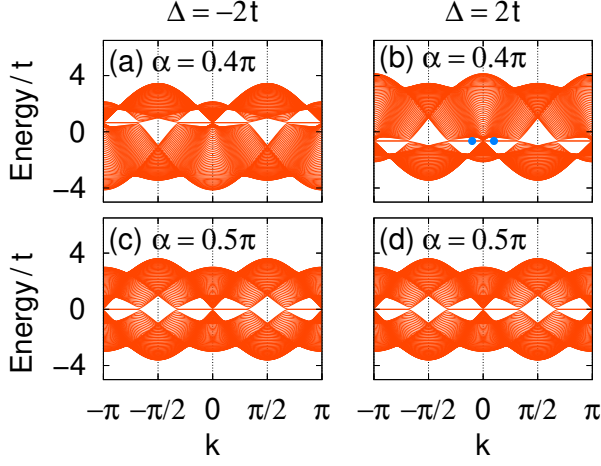


FIG. 8. Energy dispersion for a lattice with zigzag edges for finite  $\Delta$  with  $N = 71$ : (a) for  $\alpha = 0.4\pi$  and  $\Delta = -2t$ , (b) for  $\alpha = 0.4\pi$  and  $\Delta = 2t$ , (c) for  $\alpha = 0.5\pi$  and  $\Delta = -2t$ , and (d) for  $\alpha = 0.5\pi$  and  $\Delta = 2t$ . The solid circles in (b) indicate edge states in which the multipole density is evaluated in Figs. 9(b) and 9(d).

Dirac points become type-I, that is,  $\alpha > \tan^{-1} 2$ . In particular, for  $\alpha = 0.5\pi$  ( $t_1 = 0$ ), we find the zero-energy edge states except for the projected Dirac points, consistent with the non-zero values of the winding number  $w(k)$ . For an even number of  $N$ , the energy of the zero-energy states deviates from zero when  $N$  is small. Thus, we chose  $N = 71$  for the calculations presented above.

To examine the stability of the edge states against the inclusion of the level splitting, we also evaluate the energy bands for finite  $\Delta$ . In Fig. 8, we show the energy bands for  $\Delta = \pm 2t$  at  $\alpha = 0.4\pi$  and  $0.5\pi$ . While the energy of the edge states deviates from zero for  $\Delta \neq 0$  at  $\alpha \neq 0.5\pi$ , the edge states persist even for finite  $\Delta$ . These edge states are situated at  $E = -\Delta/\tan\alpha$ , corresponding to the energy at the Dirac points and the Fermi level for the half-filled case. We have checked that the edge states appear as long as the type-I Dirac points exist, that is,  $\alpha > \tan^{-1} 2$  and  $|\Delta| < 4t_2$ .

To gain further insights into the edge states, we evaluate the multipole density. The multipole operators at site  $(i, j)$  are defined as

$$\hat{\sigma}^\mu(i, j) = \sum_{\tau\tau'} c_{ij\tau}^\dagger \sigma_{\tau\tau'}^\mu c_{ij\tau'}, \quad (16)$$

where  $c_{ij\tau}$  denotes the annihilation operator of the electron at site  $(i, j)$  with orbital  $\tau$ , and  $\mu = 0, x, y, \text{ or } z$ . The multipole density operator at position  $i$  is

$$\begin{aligned} \hat{\sigma}^\mu(i) &= \sum_j \hat{\sigma}^\mu(i, j) \\ &= \sum_{k\tau\tau'} c_{ik\tau}^\dagger \sigma_{\tau\tau'}^\mu c_{ik\tau'} \\ &= \sum_k \hat{\sigma}^\mu(i, k), \end{aligned} \quad (17)$$

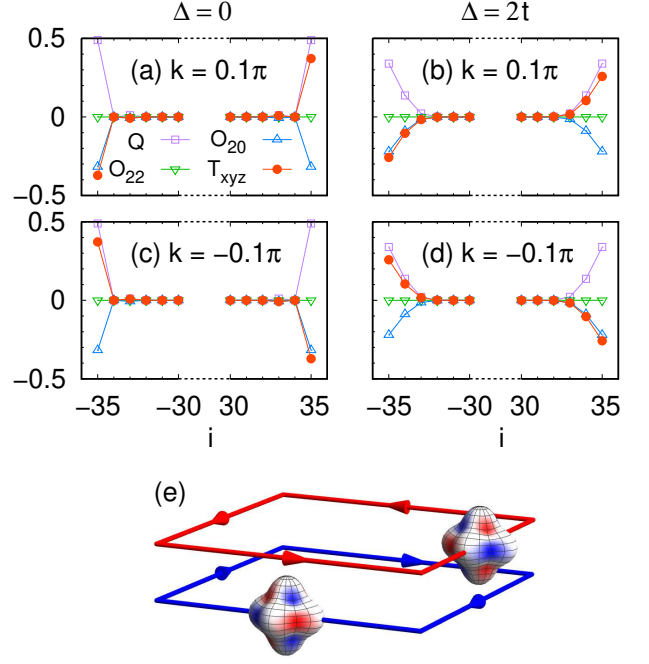


FIG. 9. Multipole density around the edges in the edge states for a lattice with zigzag edges at  $\alpha = 0.4\pi$  with  $N = 71$ : (a) for  $k = 0.1\pi$  and  $\Delta = 0$ , (b) for  $k = 0.1\pi$  and  $\Delta = 2t$ , (c) for  $k = -0.1\pi$  and  $\Delta = 0$ , and (d) for  $k = -0.1\pi$  and  $\Delta = 2t$ . (e) Schematic view of a pair of edge states with opposite momenta having octupole moments. The shape of the two objects indicates the cubic symmetric charge distribution in the wavefunctions. The red (blue) color represents the dipole moment density parallel (antiparallel) to the  $z$  direction.

where  $c_{ik\tau}$  is the Fourier transform of  $c_{ij\tau}$  along the edges. The 0th component is the charge operator  $\hat{Q}(i) = \hat{\sigma}^0(i)$ , the  $z$  and  $x$  components are the quadrupole operators  $\hat{O}_{20}(i) = \hat{\sigma}^z(i)$  and  $\hat{O}_{22}(i) = \hat{\sigma}^x(i)$ , respectively, and the  $y$  component is the octupole operator  $\hat{T}_{xyz}(i) = \hat{\sigma}^y(i)$  [47, 48].

For a lattice with zigzag edges, we can show that the eigenstate of  $\hat{\sigma}^y(-N/2, \pi/6)$  with eigenvalue  $-1$  and the eigenstate of  $\hat{\sigma}^y(N/2, \pi/6)$  with eigenvalue  $+1$  do not have matrix elements of the Hamiltonian for  $\alpha = 0.5\pi$  and  $\Delta = 0$ . Thus, these states are the zero-energy states for  $\alpha = 0.5\pi$  and  $\Delta = 0$  completely localized on the left and right edges, respectively, possessing opposite octupole moments.

For other values of  $k$ ,  $\alpha$ , and  $\Delta$ , we need to numerically evaluate the multipole density:  $Q(i) = \langle \hat{Q}(i) \rangle$ ,  $O_{20}(i) = \langle \hat{O}_{20}(i) \rangle$ ,  $O_{22}(i) = \langle \hat{O}_{22}(i) \rangle$ , and  $T_{xyz}(i) = \langle \hat{T}_{xyz}(i) \rangle$ , where  $\langle \dots \rangle$  denotes the expectation value. In Figs. 9(a)–9(d), we show the multipole density in the edge states for  $\alpha = 0.4\pi$  at  $k = \pm 0.1\pi$  with  $\Delta = 0$  and  $2t$ . The edge states are doubly degenerate, and we take the average of the two states. From the charge density  $Q$ , we recognize these states are well localized around the edges. We find that the quadrupole moment  $O_{22}$  is always zero. The



finite quadrupole moment  $O_{20}$  indicates an imbalance in the orbital occupations between  $x^2 - y^2$  and  $3z^2 - r^2$ . This moment has the same sign on both edges. The octupole moment  $T_{xyz}$  has opposite signs between the edges. The octupole moment changes its sign when we change the sign of the momentum  $k$  [compare Fig. 9(a) with Fig. 9(c) and Fig. 9(b) with Fig. 9(d)]. Thus, the edge states are helical regarding the octupole moment. In Fig.9(e), we show a schematic view of the helical octupolar edge states.

## V. SUMMARY AND DISCUSSION

We have studied an  $e_g$  orbital model on a square lattice with nearest-neighbor hopping. This model is characterized by two hopping parameters,  $t_1$  and  $t_2$ . The type of the Dirac points depends on their ratio. For the case of the type-I Dirac point, edge states appear on a lattice with zigzag edges. We find that these edge states possess helical octupolar moments.

In  $f$  electron systems, octupole order has been identified in certain materials such as  $\text{NpO}_2$  [18, 20, 21, 49–53] and  $\text{Ce}_x\text{La}_{1-x}\text{B}_6$  [54–59]. For  $e_g$  orbital systems of  $d$  electrons, the potential for octupole ordering in the bulk perovskite manganites was previously discussed [47, 60–62], but a theory incorporating fluctuations beyond the mean-field approximation concluded it is unlikely [33, 48, 63].

The present study reveals the potential emergence of the octupole moments on edges of  $e_g$  orbital systems. If a helical octupolar edge current appears for an insulator, it could be designated as a quantum octupole Hall system, analogous to a quantum spin Hall system exhibiting a helical spin edge current. Such explorations into  $e_g$  orbital systems hold promise for fostering deeper connections between topological phenomena and multipole physics.

## ACKNOWLEDGMENTS

This work was supported by JSPS KAKENHI Grant Number JP23K03330.

- 
- [1] P. R. Wallace, The Band Theory of Graphite, *Phys. Rev.* **71**, 622 (1947).
  - [2] K. S. Novoselov, A. K. Geim, S. V. Morozov, D. Jiang, M. I. Katsnelson, I. V. Grigorieva, S. V. Dubonos, and A. A. Firsov, Two-dimensional gas of massless Dirac fermions in graphene, *Nature* **438**, 197 (2005).
  - [3] S. Murakami, Phase transition between the quantum spin Hall and insulator phases in 3D: Emergence of a topological gapless phase, *New J. Phys.* **9**, 356 (2007).
  - [4] X. Wan, A. M. Turner, A. Vishwanath, and S. Y. Savrasov, Topological semimetal and Fermi-arc surface states in the electronic structure of pyrochlore iridates, *Phys. Rev. B* **83**, 205101 (2011).
  - [5] Y. A. Bychkov and E. I. Rashba, Properties of a 2D electron gas with lifted spectral degeneracy, *JETP Lett.* **39**, 78 (1984).
  - [6] K. Kubo, Weyl Semimetallic State in the Rashba–Hubbard Model, *J. Phys. Soc. Jpn.* **93**, 024708 (2024).
  - [7] C. B. Bishop, G. Liu, E. Dagotto, and A. Moreo, On-site attractive multiorbital Hamiltonian for d-wave superconductors, *Phys. Rev. B* **93**, 224519 (2016).
  - [8] M. Horio, C. E. Matt, K. Kramer, D. Sutter, A. M. Cook, Y. Sassa, K. Hauser, M. Månsson, N. C. Plumb, M. Shi, O. J. Lipscombe, S. M. Hayden, T. Neupert, and J. Chang, Two-dimensional type-II Dirac fermions in layered oxides, *Nat Commun* **9**, 3252 (2018).
  - [9] L. L. Tao and E. Y. Tsymlal, Two-dimensional type-II Dirac fermions in a  $\text{LaAlO}_3/\text{LaNiO}_3/\text{LaAlO}_3$  quantum well, *Phys. Rev. B* **98**, 121102(R) (2018).
  - [10] A. A. Soluyanov, D. Gresch, Z. Wang, Q. Wu, M. Troyer, X. Dai, and B. A. Bernevig, Type-II Weyl semimetals, *Nature* **527**, 495 (2015).
  - [11] C. L. Kane and E. J. Mele,  $Z_2$  Topological Order and the Quantum Spin Hall Effect, *Phys. Rev. Lett.* **95**, 146802 (2005).
  - [12] M. Fujita, K. Wakabayashi, K. Nakada, and K. Kusakabe, Peculiar Localized State at Zigzag Graphite Edge, *J. Phys. Soc. Jpn.* **65**, 1920 (1996).
  - [13] K. Kubo, Fulde–Ferrell–Larkin–Ovchinnikov State in the Absence of a Magnetic Field, *J. Phys. Soc. Jpn.* **77**, 043702 (2008).
  - [14] K. Kubo, Superconductivity in  $e_g$  orbital systems with multi-Fermi-surface, *J. Optoelectron. Adv. Mater.* **10**, 1683 (2008).
  - [15] J. C. Slater and G. F. Koster, Simplified LCAO Method for the Periodic Potential Problem, *Phys. Rev.* **94**, 1498 (1954).
  - [16] P. W. Anderson, New Approach to the Theory of Superexchange Interactions, *Phys. Rev.* **115**, 2 (1959).
  - [17] T. Hotta and K. Ueda, Construction of a microscopic model for f-electron systems on the basis of a j-j coupling scheme, *Phys. Rev. B* **67**, 104518 (2003).
  - [18] K. Kubo and T. Hotta, Multipole ordering in f-electron systems on the basis of a j-j coupling scheme, *Phys. Rev. B* **72**, 144401 (2005).
  - [19] K. Kubo and T. Hotta, Orbital-Controlled Superconductivity in f-Electron Systems, *J. Phys. Soc. Jpn.* **75**, 083702 (2006).
  - [20] K. Kubo and T. Hotta, Multipole ordering in f-electron systems, *Physica B* **378–380**, 1081 (2006).
  - [21] K. Kubo and T. Hotta, Multipole Ordering and Fluctuations in f-Electron Systems, *J. Phys. Soc. Jpn.* **75 Suppl.**, 232 (2006).
  - [22] K. Kubo and T. Hotta, Superconductivity in f-electron systems controlled by crystalline electric fields, *J. Magn. Magn. Mater.* **310**, 572 (2007).
  - [23] K. Kubo and T. Hotta, Influence of lattice structure on multipole interactions in  $\Gamma_3$  non-Kramers doublet systems, *Phys. Rev. B* **95**, 054425 (2017).
  - [24] K. Kubo and T. Hotta, Multipole interactions of  $\Gamma_3$  non-Kramers doublet systems on cubic lattices,

- J. Phys.: Conf. Ser. **969**, 012096 (2018).
- [25] K. Kubo, Anisotropic Superconductivity Emerging from the Orbital Degrees of Freedom in a  $\Gamma_3$  Non-Kramers Doublet System, J. Phys. Soc. Jpn. **87**, 073701 (2018).
- [26] K. Kubo, Superconductivity in a multiorbital model for the  $\Gamma_3$  crystalline electric field state, AIP Adv. **8**, 101313 (2018).
- [27] K. Kubo, Nematic and time-reversal breaking superconductivities coexisting with quadrupole order in a  $\Gamma_3$  system, Phys. Rev. B **101**, 064512 (2020).
- [28] K. Kubo, Coexistence of Superconductivity with Quadrupole Order in a  $\Gamma_3$  System, JPS Conf. Proc. **30**, 011041 (2020).
- [29] S. Ishihara, J. Inoue, and S. Maekawa, Electronic structure and effective Hamiltonian in perovskite Mn oxides, Physica C **263**, 130 (1996).
- [30] S. Ishihara, J. Inoue, and S. Maekawa, Effective Hamiltonian in manganites: Study of the orbital and spin structures, Phys. Rev. B **55**, 8280 (1997).
- [31] J. van den Brink, P. Horsch, F. Mack, and A. M. Oleś, Orbital dynamics in ferromagnetic transition-metal oxides, Phys. Rev. B **59**, 6795 (1999).
- [32] K. Kubo, Quantum Fluctuation Induced Order in an Anisotropic Pseudospin Model, J. Phys. Soc. Jpn. **71**, 1308 (2002).
- [33] K. Kubo and D. S. Hirashima, Orbital orderings and excitations in ferromagnetic metallic manganites, J. Phys. Chem. Solids **63**, 1571 (2002).
- [34] A. Kitaev, Anyons in an exactly solved model and beyond, Ann. Phys. (N.Y.) **321**, 2 (2006).
- [35] G. Jackeli and G. Khaliullin, Mott Insulators in the Strong Spin-Orbit Coupling Limit: From Heisenberg to a Quantum Compass and Kitaev Models, Phys. Rev. Lett. **102**, 017205 (2009).
- [36] K. Kubo, Pairing symmetry in a two-orbital Hubbard model on a square lattice, Phys. Rev. B **75**, 224509 (2007).
- [37] P. Fulde and R. A. Ferrell, Superconductivity in a Strong Spin-Exchange Field, Phys. Rev. **135**, A550 (1964).
- [38] A. I. Larkin and Y. N. Ovchinnikov, Inhomogeneous state of superconductors, Sov. Phys. JETP **20**, 762 (1965).
- [39] C. N. Yang,  $\eta$  pairing and off-diagonal long-range order in a Hubbard model, Phys. Rev. Lett. **63**, 2144 (1989).
- [40] H. Huang, K.-H. Jin, and F. Liu, Black-hole horizon in the Dirac semimetal  $\text{Zn}_2\text{In}_2\text{S}_5$ , Phys. Rev. B **98**, 121110(R) (2018).
- [41] H. Liu, J.-T. Sun, C. Cheng, F. Liu, and S. Meng, Photoinduced Nonequilibrium Topological States in Strained Black Phosphorus, Phys. Rev. Lett. **120**, 237403 (2018).
- [42] I. M. Lifshitz, Anomalies of electron characteristics of a metal in the high pressure region, Sov. Phys. JETP **11**, 1130 (1960).
- [43] K. Sun, W. V. Liu, A. Hemmerich, and S. Das Sarma, Topological semimetal in a fermionic optical lattice, Nat. Phys. **8**, 67 (2012).
- [44] J.-M. Hou, Hidden-Symmetry-Protected Topological Semimetals on a Square Lattice, Phys. Rev. Lett. **111**, 130403 (2013).
- [45] S. Ryu and Y. Hatsugai, Topological Origin of Zero-Energy Edge States in Particle-Hole Symmetric Systems, Phys. Rev. Lett. **89**, 077002 (2002).
- [46] Y. Hatsugai, Bulk-edge correspondence in graphene with/without magnetic field: Chiral symmetry, Dirac fermions and edge states, Solid State Commun. **149**, 1061 (2009).
- [47] A. Takahashi and H. Shiba, Possible Orbital Orderings in a Model of Metallic Double-Exchange Ferromagnets, J. Phys. Soc. Jpn. **69**, 3328 (2000).
- [48] K. Kubo and D. S. Hirashima, Orbital Orderings in Ferromagnetic Metallic Manganites, J. Phys. Soc. Jpn. **71**, 183 (2002).
- [49] J. A. Paixão, C. Detlefs, M. J. Longfield, R. Caciuffo, P. Santini, N. Bernhoeft, J. Rebizant, and G. H. Lander, Triple-q Octupolar Ordering in  $\text{NpO}_2$ , Phys. Rev. Lett. **89**, 187202 (2002).
- [50] R. Caciuffo, J. A. Paixão, C. Detlefs, M. J. Longfield, P. Santini, N. Bernhoeft, J. Rebizant, and G. H. Lander, Multipolar ordering in  $\text{NpO}_2$  below 25 K, J. Phys.: Condens. Matter **15**, S2287 (2003).
- [51] Y. Tokunaga, Y. Homma, S. Kambe, D. Aoki, H. Sakai, E. Yamamoto, A. Nakamura, Y. Shiokawa, R. E. Walstedt, and H. Yasuoka, NMR Evidence for Triple-q Multipole Structure in  $\text{NpO}_2$ , Phys. Rev. Lett. **94**, 137209 (2005).
- [52] K. Kubo and T. Hotta, Microscopic theory of multipole ordering in  $\text{NpO}_2$ , Phys. Rev. B **71**, 140404(R) (2005).
- [53] K. Kubo and T. Hotta, Analysis of f-p model for octupole ordering in  $\text{NpO}_2$ , Phys. Rev. B **72**, 132411 (2005).
- [54] K. Kubo and Y. Kuramoto, Lattice Distortion and Octupole Ordering Model in  $\text{Ce}_x\text{La}_{1-x}\text{B}_6$ , J. Phys. Soc. Jpn. **72**, 1859 (2003).
- [55] K. Kubo and Y. Kuramoto, Octupole Ordering Model for the Phase IV of  $\text{Ce}_x\text{La}_{1-x}\text{B}_6$ , J. Phys. Soc. Jpn. **73**, 216 (2004).
- [56] T. Morie, T. Sakakibara, T. Tayama, and S. Kunii, Low-Temperature Magnetization Study on the Phase IV Ordering in  $\text{Ce}_x\text{La}_{1-x}\text{B}_6$  under [111] Uniaxial Pressures, J. Phys. Soc. Jpn. **73**, 2381 (2004).
- [57] D. Mannix, Y. Tanaka, D. Carbone, N. Bernhoeft, and S. Kunii, Order Parameter Segregation in  $\text{Ce}_{0.7}\text{La}_{0.3}\text{B}_6$ : 4f Octopole and 5d Dipole Magnetic Order, Phys. Rev. Lett. **95**, 117206 (2005).
- [58] H. Kusunose and Y. Kuramoto, Evidence for Octupole Order in  $\text{Ce}_{0.7}\text{La}_{0.3}\text{B}_6$  from Resonant X-ray Scattering, J. Phys. Soc. Jpn. **74**, 3139 (2005).
- [59] K. Kuwahara, K. Iwasa, M. Kohgi, N. Aso, M. Sera, and F. Iga, Detection of Neutron Scattering from Phase IV of  $\text{Ce}_{0.7}\text{La}_{0.3}\text{B}_6$ : A Confirmation of the Octupole Order, J. Phys. Soc. Jpn. **76**, 093702 (2007).
- [60] R. Maezono and N. Nagaosa, Complex orbital state in manganites, Phys. Rev. B **62**, 11576 (2000).
- [61] J. van den Brink and D. Khomskii, Orbital ordering of complex orbitals in doped Mott insulators, Phys. Rev. B **63**, 140416(R) (2001).
- [62] D. I. Khomskii, ORBITAL EFFECTS IN MANGANITES, Int. J. Mod. Phys. B **15**, 2665 (2001).
- [63] K. Kubo and D. S. Hirashima, Correlation Effect on Orbital Orderings in Ferromagnetic Metallic Manganites, J. Phys. Soc. Jpn. **71** Suppl., 151 (2002).